Preparation and Performance Study of Fe_2O_3/Geopolymer Porous Ceramics

Zhenfan CHEN [1], Shaofeng ZHU [2] *, Qingqing WANG [1]

[1] *School of Materials Science and Chemical Engineering, Anhui Jianzhu University, Hefei, Anhui 230601, China*
[2] *Anhui Engineering Research Center for Building Energy Conservation, Hefei, Anhui 230022, China*

http://doi.org/10.5755/j02.ms.35956

Received 6 January 2024; accepted 18 March 2024

In this paper, a kind of geopolymer porous ceramic was prepared using the physical foaming method combined with the gel casting process. The effect of sintering temperature on phase composition and physical properties of samples was studied. Fe_2O_3/geopolymer porous ceramic samples were prepared by Fe_2O_3 loaded on the surface of geopolymer porous ceramic samples through the impregnation-calcination method. The Fe_2O_3-loaded geopolymer porous ceramic samples were characterized by SEM-EDS, FTIR, and XPS. The adsorption experiments were employed to investigate the effect of testing conditions on the adsorption of Pb(II) from the $Pb(NO_3)_2$ solution. The results show that the porosity of geopolymer porous ceramic samples decreased while the compressive strength increased, and the proportion of pores with a pore size range of < 0.1 mm and 0.1 mm – 0.2 mm increased. The adsorption capacity and removal rate of Pb(II) first increased and then decreased with the increase of $Fe(NO_3)_3$ solution concentration, calcination temperature, and holding time. The adsorption capacity and removal rate of Pb(II) increased with the increase of the pH value and the initial Pb(II) concentration of the solution.

Keywords: geopolymer, porous ceramics, Fe_2O_3, adsorption.

1. INTRODUCTION

With the growth of the population and the development of industrialization, heavy metal pollution become an increasing global problem. Lead (Pb) and its alloys have been used in producing lead-acid batteries, paints, cables, and ammunition [1]. The extensive use of Pb inevitably causes pollution to groundwater, causing a large amount of Pb to enter the human being and accumulation. When the concentration of Pb within the human being exceeds a certain level, the organs and tissues of humans will be destroyed [2]. The list of carcinogens published by the International Agency for Research on Cancer of the World Health Organization lists Pb as a Class 2B carcinogen. And it is included in the first batch of toxic and harmful water pollutant lists.

At present, the main methods for the removal of Pb(II) include chemical precipitation [3], ion-exchange [4], membrane separation [5], and adsorption [6]. Among these, the adsorption method has been widely used due to its low cost and excellent adsorptive properties, especially for dilute solutions [7]. The selection of adsorbents is a crucial step in adsorption method, including organic adsorbents such as activated carbon [8], carbon nanotubes [9], polysaccharides [10], as well as inorganic adsorbents such as clay [11] and metallic oxide [12]. Fe_2O_3 is one of the ideal adsorption materials, which not only has abundant pore structures but also possesses a large number of sites and surface functional groups. Therefore, Fe_2O_3 exhibits excellent activity for the adsorption and degradation of various inorganic substances [13]. However, the particle size of Fe_2O_3 is small, making it difficult to recover after being used. Therefore, the adsorbent or the active component of the adsorbent is considered to be loaded on the carriers, such as hydrogels or porous ceramics [14]. The geopolymer porous ceramic samples prepared by sintering the porous geopolymer have numerous advantages, such as large specific surface area, good chemical stability, and mechanical properties [15].

In this paper, the geopolymer porous ceramic samples were prepared by the physical foaming method combined with a gel casting process using metakaolin and potassium silicate solution as the main raw materials. The effect of sintering temperature on the phase composition, physical properties, and pore size distribution of geopolymer porous ceramic samples was studied. Fe_2O_3/geopolymer porous ceramic samples were prepared by the Fe_2O_3 loading on the surface of the geopolymer porous ceramic samples using the impregnation-calcination method. At the same time, the adsorption performance of Fe_2O_3/geopolymer porous ceramics samples for Pb(II) from $Pb(NO_3)_2$ solution was also studied.

2. MATERIALS AND METHODS

2.1. Raw materials

The solid raw material used in the experiment was metakaolin, made by calcining kaolin (Industrial pure, Tianjin Zhiyuan Chemical Reagent Co., Ltd., China) at 800°C. The average particle size and specific surface area of metakaolin were 8.5 μm and 0.43 m^2/g. The molar ratio of SiO_2 to K_2O in the potassium silicate solution (Chemically pure, Zhengzhou Borun Chemical Reagent Co., Ltd., China) used in the experiment was 3.3. The $Fe(NO_3)_3 \cdot 9H_2O$

* Corresponding author. Tel.: +086-13965020668; fax: + 0551-63517457
E-mail: *zhusf@ahjzu.edu.cn* (S. Zhu)

(Tianjin Zhiyuan Chemical Reagent Co., Ltd., Chian) and $Pb(NO_3)_2$ (Shanghai Aladdin Biochemical Technology Co., Ltd., China) used were both chemically pure.

2.2. Experimental method

2.2.1. Preparation of geopolymer porous ceramic samples

The KOH solution of 12M was added to the potassium silicate solution to adjust the molar ratio of SiO_2 and K_2O to 1.2, and the alkali activator solution was obtained. 1.91 g polyacrylic acid and 32 g metakaolin were added to 22.4 g alkali activator solution and stirred for 30 minutes at 500 rpm to obtain the geopolymer slurry. 2.6 g coconut diethanolamide was added to the geopolymer slurry, and stirred at 800 rpm for 7 minutes, and then 1.9 g calcium oxide (CaO) was added to the geopolymer slurry and stirred for 3 minutes. The geopolymer slurry was injected into the mold and cured at 70℃ for 24 hours. After demolding and then drying, the geopolymer porous ceramic green bodies were obtained. The green bodies were placed into a high-temperature furnace heated to the predetermined temperature to obtain geopolymer porous ceramic samples.A new paragraph must be indented in the first line by 0.6 cm.

2.2.2. Preparation of Fe_2O_3/geopolymer porous ceramic samples

The geopolymer porous ceramic samples were crushed to obtain block geopolymer porous ceramic particles with a size of approximately 1 – 3 mm. The geopolymer porous ceramic particles were placed in deionized water, cleaned with ultrasound for 10 minutes, and then dried. The cleaned geopolymer porous ceramic particles were immersed in a 2M HNO_3 solution for 2 hours. Finally, they were taken out and washed repeatedly with deionized water to obtain the activated geopolymer porous ceramic particles.

After activation treatment, the geopolymer porous ceramic particles were impregnated in $Fe(NO_3)_3$ solution with a certain concentration for 24 hours and dried. Then the samples were calcined at a predetermined temperature for a certain holding time to prepare Fe_2O_3/geopolymer porous ceramic samples.

2.2.3. Determination of Fe_2O_3 load capacity on Fe_2O_3/geopolymer porous ceramic samples

The Fe_2O_3 loaded on the surface of Fe_2O_3/geopolymer porous ceramic samples was dissolved in a HNO_3 solution. After dissolution, the content of iron ions in the HNO_3 solution was determined by atomic absorption spectrophotometer, and the Fe_2O_3 load capacity of the Fe_2O_3/geopolymer porous ceramic samples was calculated, as shown in Eq 1:

$$Q = \frac{C_d \cdot V_d}{m}, \quad (1)$$

where Q represents the Fe_2O_3 load capacity of the Fe_2O_3/geopolymer porous ceramic samples (mg/g); C_d represents the concentration of iron ions in the HNO_3 solution after dissolution (mg/L); m represents the mass of Fe_2O_3/geopolymer porous ceramic samples(g); V_d represents the volume of HNO_3 solution (L).

2.2.4. Pb(II) adsorption experiments of Fe_2O_3/geopolymer porous ceramic samples

The wastewater solution containing Pb(II) was simulated with an aqueous $Pb(NO_3)_2$ solution. The Fe_2O_3/geopolymer porous ceramic samples was put into the $Pb(NO_3)_2$ solution at a dosages of 1g/50ml. The solution was stirred at 120 rpm on a magnetic stirrer at constant temperature. The residual concentration of Pb(II) in the solution was determined by atomic absorption spectrophotometer and the Pb(II) adsorption capacity and removal rate of Fe_2O_3/geopolymer porous ceramic samples were calculated as shown in Eq 2 and Eq. 3:

$$\varphi = \frac{C_0 - C}{C_0} \times 100\%; \quad (2)$$

$$q = \frac{C_0 - C}{m} V, \quad (3)$$

where φ represents the removal rate (%); C_0 and C represent the initial and equilibrium concentrations (mg/L) of Pb(II) in aqueous solutions; q represents the adsorption capacity (mg/g), V represents the volume of Pb(II) solution (L), and m represents the mass of Fe_2O_3/geopolymer porous ceramic samples (g).

2.3. Characterization

The open porosity of the samples was measured by the Archimedes drainage method. The compressive strength of the samples was tested by compression testing device (JBC-LY, Shenyang Hexing Co., Ltd., China). The cross-section from the middle of the samples was cut, grounded and polished, and then observed under a stereomicroscope (XTL-30C, Shanghai Pudan Optical Instrument Co., Ltd., China). The images were analyzed by Image-pro Plus software to count the number and size of pores to obtain the pore size distribution. The microstructures of the samples were characterized by a scanning electron microscope (SEM, SU8020, Hitachi Co., Ltd., Japan). All SEM images were sprayed with Pt coating for facilitating to image. The phases of samples were determined by X-ray diffractometer (XRD, D8-Advance, Bruker Co., Ltd., Germany) using Cu K_a radiation (λ = 1.5406 Å). The composition of samples was analyzed by energy-dispersive X-ray spectroscopy (EDS, Inca Energy-350, Oxford Co., Ltd., Britain). The functional groups of the samples were analyzed by using Fourier transform infrared spectroscopy (FTIR, GD26-FTIR-650, Beijing Haifuda Technology Co., Ltd., China). The X-ray photoelectron spectroscopy (XPS, ESCALAB 250Xi, Thermo Fisher Co., Ltd., USA) with AlK_α X-ray source (hv = 1486.7 eV) was used to determine the chemical state of the sample. The X-ray beam size was 500 μm. The analysis began with survey acquisition at 100 eV of pass energy and 1 eV of step size, followed by high-resolution scans of the regions C1s,Fe2p, Pb4f and O1s at 30 eV of pass energy and a step size of 0.5 eV. All data of XPS were processed by Avantage software. All the spectra were calibrated reference to a C1s peak positioned at 284.8 eV to correct for charging effects. During the fitting process, we assume that the single-component lines have the shape of the product of Lorentzian and Gaussian component curves. Smart background was used and fitting was performed with Lorentzian/Gaussian mixed ratio of 30 %.

The concentration of Pb(II) before and after adsorption was analyzed by an atomic adsorption spectrometer (AAS, A3, Beijing Puxi Co., Ltd., China). The potential of samples was tested by the zeta potential meter (Nano ZSE, Malvern Co., Ltd., Britain).

3. RESULTS AND DISCUSSION

3.1. Characterization of geopolymer porous ceramic samples

3.1.1. Effect of sintering temperature on phase composition of geopolymer porous ceramic samples

The XRD patterns of the samples after sintering at 900 ℃ ~ 1200 ℃ are displayed in Fig. 1. The samples were composed of the amorphous and quartz phases when sintered at 900 ℃. After the samples were sintered at 950 ℃, the kaliophilite ($K_2O{\cdot}Al_2O_3{\cdot}2SiO_2$) phase began to appear in the XRD patterns. After the samples were sintered at 1000 ℃, the kaliophilite phase disappeared, and the leucite phase($K_2O{\cdot}Al_2O_3{\cdot}4SiO_2$) appeared. After being sintered at 1100 ℃, the anorthite ($CaO{\cdot}Al_2O_3{\cdot}2SiO_2$) phase appeared.

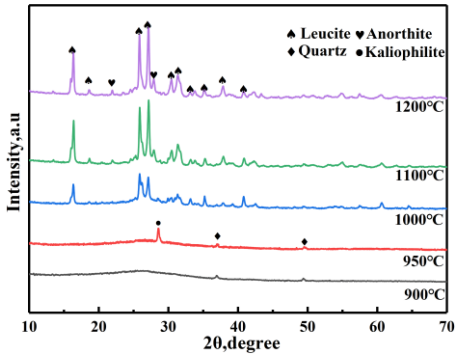

Fig. 1. XRD patterns of geopolymer porous ceramic samples at different sintering temperatures

After being sintered at 1200 ℃, there was no change in the phase composition except for the enhancement of diffraction peak intensity of the leucite phase and anorthite phase. The reaction formula for generating leucite and anorthite are shown in Eq. 4 [16, 17] and Eq. 5 [18]:

$$K_2O+Al_2O_3{\cdot}2SiO_2+2SiO_2 \rightarrow K_2O{\cdot}Al_2O_3{\cdot}4SiO_2; \quad (4)$$

$$Al_2O_3{\cdot}2SiO_2+CaO \rightarrow CaO{\cdot}Al_2O_3{\cdot}2SiO_2. \quad (5)$$

3.1.2. Effect of sintering temperature on physical properties and pore size distribution of geopolymer porous ceramic samples

The physical properties and pore size distribution of the samples at different sintering temperatures are shown in Fig. 2 and Fig. 3. With the increase of sintering temperature, the porosity of the samples gradually decreased while the compressive strength gradually increased. The average pore sizes of the samples decreased, and the proportion of pores with a pore size range of < 0.1 mm and 0.1 mm – 0.2 mm increased.

On the one hand, the amorphous geopolymers will undergo significant sintering shrinkage when they are transformed into crystalline phases [16, 19]. On the other hand, with the increase in sintering temperature, the amount of liquid phase generated in the K_2O-Al_2O_3-SiO_2 system [16] gradually increases during the sintering process.

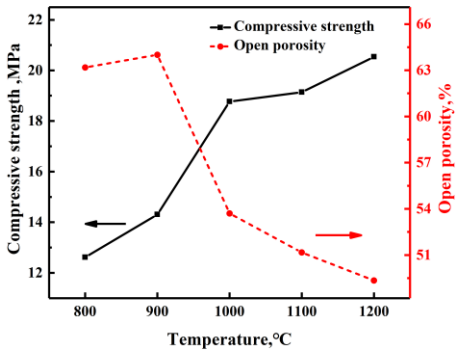

Fig. 2. Effects of sintering temperature on physical properties of geopolymer porous ceramic samples

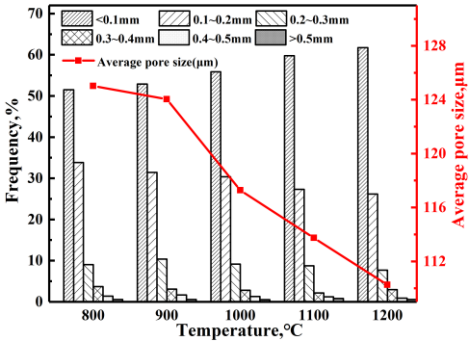

Fig. 3. Pore size distribution and average pore size of geopolymer porous ceramic samples at different sintering temperatures

Its fluidity also gradually increases, which is conducive to the densification of the samples and the crystallization of the leucite phase with high-strength. Therefore, as the sintering temperature increased, the pore size of the pores gradually decreased. Some of the pores were closed, leading to a decrease in the open porosity. The generating of the leucite phase caused an increase of compressive strength.

3.2. Preparation and characterization of Fe_2O_3/geopolymer porous ceramic samples

3.2.1. Effect of the calcination temperature and holding time of Fe_2O_3/geopolymer porous ceramic samples

Based on previous research, crystalline water in $Fe(NO_3)_3{\cdot}9H_2O$ is removed at about 150 ℃ and $Fe(NO_3)_3$ is decomposed into Fe_2O_3 completely until 300 ℃, as shown in Eq. 6 and Eq. 7 [20]. Therefore, the calcination temperature was chosen from 350 ℃ to 650 ℃, the holding time was chosen from 1 hour to 6 hours in the preparation process of Fe_2O_3/geopolymer porous ceramic samples.

$$Fe(NO_3)_3{\cdot}9H_2O \rightarrow Fe(NO_3)_3+9H_2O; \quad (6)$$

$$4\ Fe(NO_3)_3 \rightarrow 2Fe_2O_3+12NO+3O_2. \quad (7)$$

The SEM images of the samples calcined at different temperatures for 2 hours are shown in Fig. 4, Fig. 5, and Fig. 6. After being calcined at 350 ℃, there were fewer Fe_2O_3 particles on the surface of the samples, and the Fe_2O_3 particles were tiny. After being calcined at 450 ℃, the number of Fe_2O_3 particles on the surface increased

significantly and the distribution of Fe_2O_3 particles was uniform.

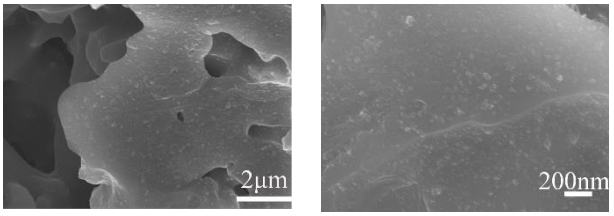

a b

Fig. 4. SEM images of Fe_2O_3/geopolymer porous ceramic samples prepared by calcining at 350℃ for 2 hours: a – ×5000 magnification; b – ×50000 magnification

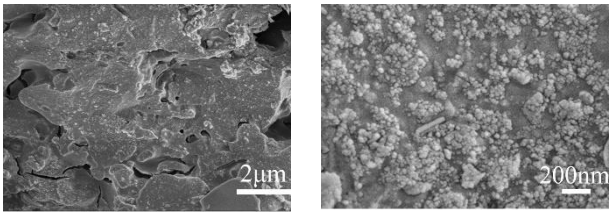

a b

Fig. 5. SEM images of Fe_2O_3/geopolymer porous ceramic samples prepared by calcining at 450℃ for 2 hours: a – ×5000 magnification; b – ×50000 magnification

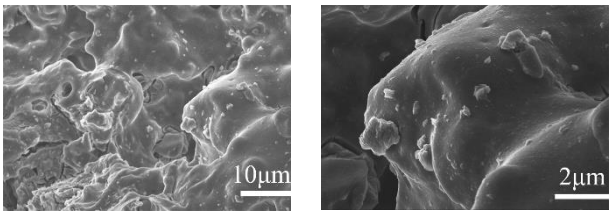

a b

Fig. 6. SEM images of Fe_2O_3/geopolymer porous ceramic samples prepared by calcining at 650℃ for 2 hours: a – ×1000 magnification; b – ×5000 magnification

The size of the Fe_2O_3 particles increased, ranging from tens to one hundred nanometers. However, when the calcination temperature increased to 650 ℃, the Fe_2O_3 particles were dispersively distributed on the surface of the samples. The particle size of Fe_2O_3 further increased, ranging from several hundred nanometers to two micrometers.

The SEM images of the samples calcined at 450 ℃ for different holding time are shown in Fig. 5, Fig. 7, and Fig. 8.

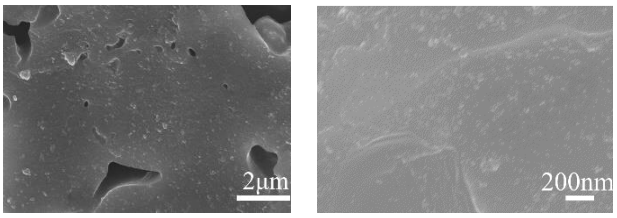

a b

Fig. 7. SEM images of Fe_2O_3/geopolymer porous ceramic samples prepared by calcining at 450℃ for 1 hour: a – ×5000 magnification; b – ×50000 magnification

The effect of holding time on the particle size and distribution of Fe_2O_3 was consistent with the calcination temperature. In addition, after being calcined at 450 ℃ for 6 hours, some of the Fe_2O_3 particles on the surface agglomerated.

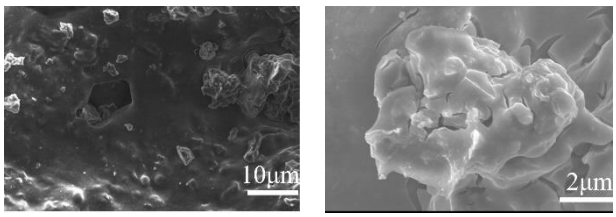

a b

Fig. 8. SEM images of Fe_2O_3/geopolymer porous ceramic samples prepared by calcining at 450℃ for 6 hours: a – ×1000 magnification; b – ×5000 magnification

3.2.2. Effect of $Fe(NO_3)_3$ solution concentration on Fe_2O_3/geopolymer porous ceramic samples

The SEM images of the surface of Fe_2O_3/geopolymer porous ceramic samples papered by impregnating with 0.1M, 0.2M, and 0.6M $Fe(NO_3)_3$ solution are shown in Fig. 9, Fig. 10, and Fig. 11. When the concentration of $Fe(NO_3)_3$ was 0.1M, as shown in Fig. 9, there were fewer Fe_2O_3 particles loaded on the surface of samples.

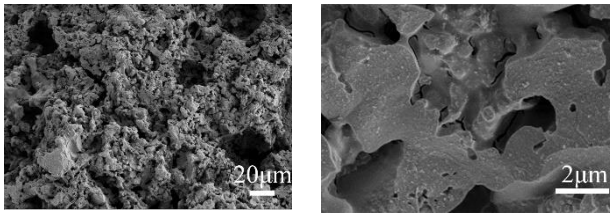

a b

Fig. 9. SEM images of Fe_2O_3/geopolymer porous ceramic samples prepared by impregnating in 0.1M $Fe(NO_3)_3$: a – ×1000 magnification; b – ×5000 magnification

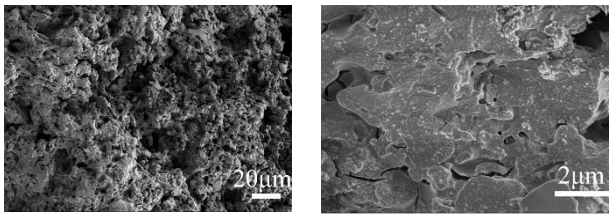

a b

Fig. 10. SEM images of Fe_2O_3/geopolymer porous ceramic samples prepared by impregnating in 0.2M $Fe(NO_3)_3$: a – ×1000 magnification; b – ×5000 magnification

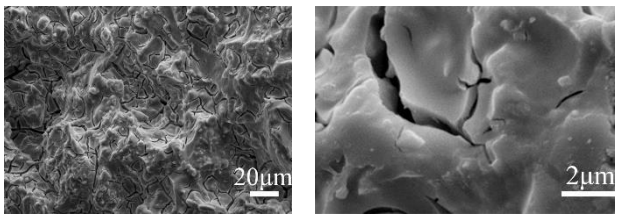

a b

Fig. 11. SEM images of Fe_2O_3/geopolymer porous ceramic samples prepared by impregnating in 0.6M $Fe(NO_3)_3$: a – ×1000 magnification; b – ×5000 magnification

When the concentration of $Fe(NO_3)_3$ increased to 0.2M, as shown in Fig. 10, the number of Fe_2O_3 particles loaded

on the surface of samples significantly increased. When the concentration of $Fe(NO_3)_3$ increased to 0.6M, as shown in Fig. 11, a large amount of Fe_2O_3 accumulated on the surface of the samples, and some pores in the samples were blocked and covered.

The SEM images and EDS patterns of samples before and after Fe_2O_3 loaded are shown in Fig. 12.

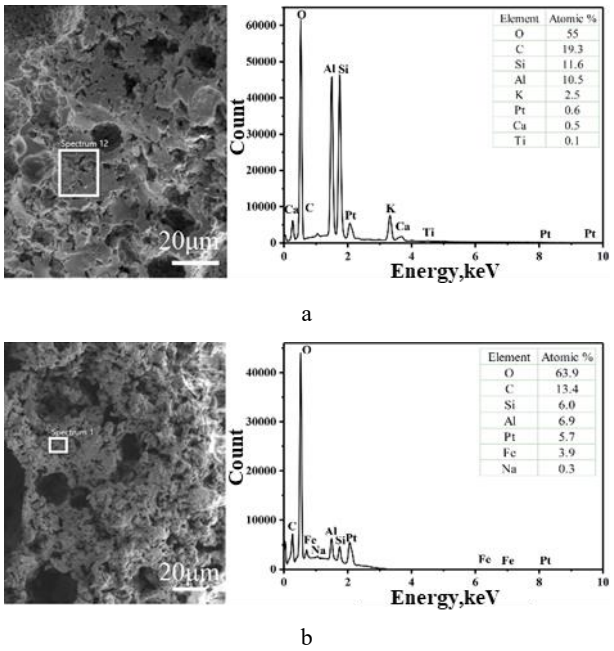

Fig. 12. SEM images and EDS patterns: a – geopolymer porous ceramic samples; b – Fe_2O_3/geopolymer porous ceramic samples

Geopolymer porous ceramic samples were mainly composed of Si, Al, and O. After loading with Fe_2O_3, the elemental peaks of Fe appeared in the EDS patterns, indicating that Fe_2O_3 was successfully loaded on the surface of geopolymer porous ceramic samples.

3.3. Pb(II) adsorption performance of Fe_2O_3/geopolymer porous ceramic samples

3.3.1. Effect of the calcination temperature and holding time on the adsorption performance of Pb(II)

The effect of the calcination temperature on the Pb(II) adsorption capacity and removal rate of samples is shown in Fig. 13. With the increase of calcination temperature, the adsorption capacity and removal rate of Pb(II) increased first and then decreased. When the samples were calcined at 450 °C, their adsorption capacity and removal rate of Pb(II) reached maximum. As shown in Fig. 14, the effect of holding time on Pb(II) adsorption capacity and removal rate of samples showed the same trend. The adsorption capacity increased firstly then decreased with the extension of holding time. When the samples were calcined for 2 hours, their adsorption capacity of Pb(II) reached maximum.

As shown in Fig. 4 and Fig. 7 when the samples were prepared by calcined at high temperature or calcined for a long holding time, the surface of the samples had fewer Fe_2O_3 particles, and their particle size was small, resulting in a small specific surface area of Fe_2O_3 particles. Therefore, the available adsorption sites were scarce, and the adsorption capacity of Fe_2O_3/geopolymer porous ceramic samples was poor.

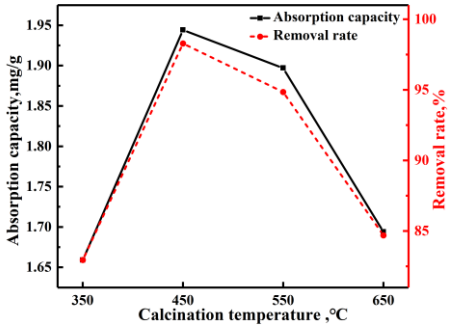

Fig. 13. Effect of calcination temperature on absorption performance of Pb(II)

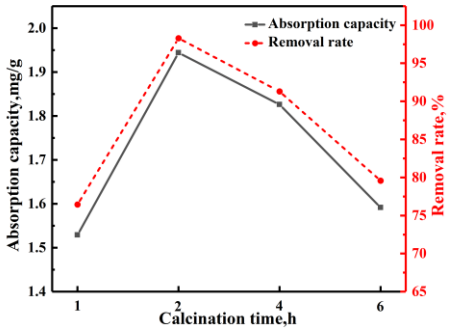

Fig. 14. Effect of calcination time on absorption performance of Pb(II)

However, when the samples were prepared by calcined at high temperature or calcined for a long holding time, as shown in Fig. 6 and Fig. 8. The Fe_2O_3 particles on the surface of the samples were larger, which may block some tiny pores. Additionally, the agglomeration among the Fe_2O_3 particles has occurred, which led to a decrease in their number and specific surface area. The adsorption performance of the samples was weakened.

3.3.2. Effect of Fe $(NO_3)_3$ solution concentration on the adsorption performance of Fe_2O_3/geopolymer porous ceramic samples

The effect of $Fe(NO_3)_3$ solution concentration on the Fe_2O_3 load capacity of Fe_2O_3/geopolymer porous ceramic samples is shown in Fig. 15.

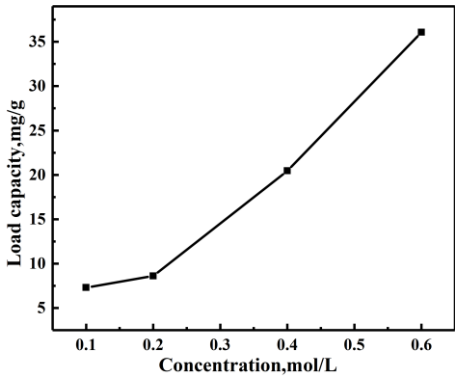

Fig. 15. Effect of $Fe(NO_3)_3$ solution concentration on Fe_2O_3 load capacity

With the concentration of $Fe(NO_3)_3$ solution increased, the Fe_2O_3 load capacity of geopolymer porous ceramic

samples gradually increased, and the load amount of Fe_2O_3 on the surface of samples gradually increased too. The effect of $Fe(NO_3)_3$ solution concentration on the Pb(II) adsorption capacity and removal rate of samples are shown in Fig.16.

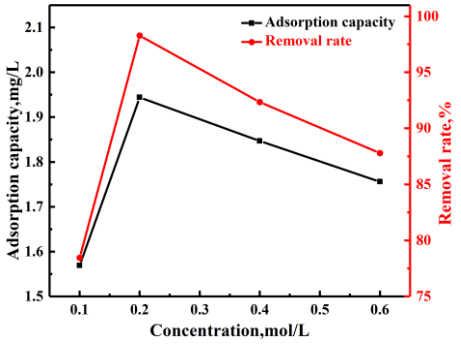

Fig. 16. Effect of $Fe(NO_3)_3$ solution concentration on absorption performance of Pb(II)

The removal rate and adsorption capacity of Pb(II) increased firstly and then decreased with the increase of $Fe(NO_3)_3$ solution concentration. When the concentration of $Fe(NO_3)_3$ solutions reached 0.2M, the Pb(II) removal rate and adsorption capacity of the samples reached maximum.

As shown in Fig. 15 and Fig. 9, Fig. 10, and Fig. 11, a high occurrence of Fe_2O_3 on the surface of samples with the increase of $Fe(NO_3)_3$ solution concentration, can provide more adsorption sites to improve adsorption capacity during the adsorption process. However, the impregnation with a high concentration of $Fe(NO_3)_3$ solution during the prepared process caused the pores on the surface of the samples to be blocked and covered. The synergistic effect between the catalyst and the porous ceramic carrier was weakened, which led to decrease in adsorption efficiency.

3.3.3. Effect of solution pH value on the adsorption performance of Pb(II)

At the initial Pb(II) concentration of 40 mg/L, the effect of solution pH value on the adsorption of Pb(II) is shown in Fig. 17. The Pb(II) adsorption capacity and removal rate of samples increased with the increase of solution pH value.

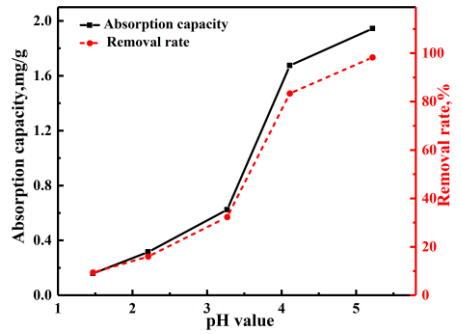

Fig. 17. Effect of Pb(II) solution pH value on absorption performance of Pb(II)

As shown in Fig. 18, when the pH value was low, the surface of the samples was positively charged and the electrostatic repulsive force limited the adsorption of Pb(II). In addition, there was competitive adsorption between H^+ and Pb(II) at a low pH value, which also led to a decrease in adsorption capacity. With the increase of pH value, the surface potential of the samples changed from positive to negative, which was conducive to the adsorption of Pb(II) with positively charged.

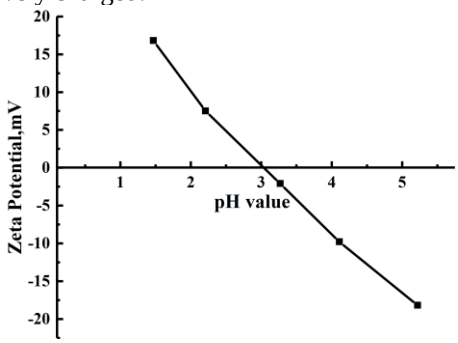

Fig. 18. Zeta potential of Fe_2O_3/geopolymer porous ceramic samples at different pH values

When the pH value was 5.22, the Pb(II) adsorption capacity and removal rate of Pb(II) reached the maximum, which was 1.944 mg/g and 98.28 %.

3.3.4. Effect of Pb(II) solution initial concentration on the adsorption performance of Pb(II)

The effect of initial Pb(II) concentration on the adsorption of Pb(II) at pH value of 5.22 is shown in Fig. 19. The adsorption capacity increased with the increasing initial concentration of Pb(II).

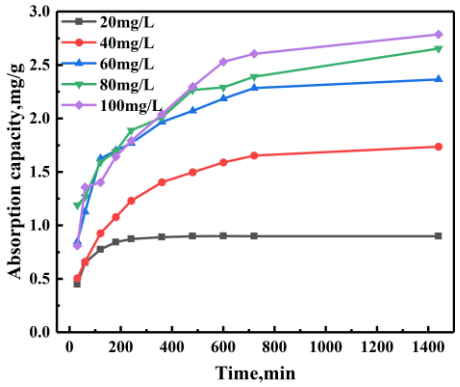

Fig. 19. Effect of Pb(II) solution initial concentration on adsorption performance of Pb(II)

When the initial concentration was 20 mg/L or 40 mg/L, the number of Pb(II) adsorbed was lower than the number of available adsorption sites. A larger number of adsorption sites remained unutilized after the adsorption of Pb(II), so the adsorption capacity of samples was low. The adsorption equilibrium time was also reduced. In a solution with an initial concentration of 20 mg/L, adsorption equilibrium was reached after only 240 minutes. When the initial concentration reached 60 mg/L or above, the Pb(II) number relative to the adsorption sites gradually increased. At this point, it was difficult for a limited number of active sites to fully adsorbed Pb (II) in the solution, and these active sites quickly tended to saturate during the adsorption process. Although the adsorption capacity still increased, the amplitude decreased. In a solution with an initial concentration of 100 mg/L, the final adsorption capacity reached the maximum, of 2.7866 mg/g. The SEM images and EDS patterns of the surface of Fe_2O_3/ geopolymer porous ceramic samples after adsorption of Pb(II) are shown in Fig. 20 and Fig. 21.

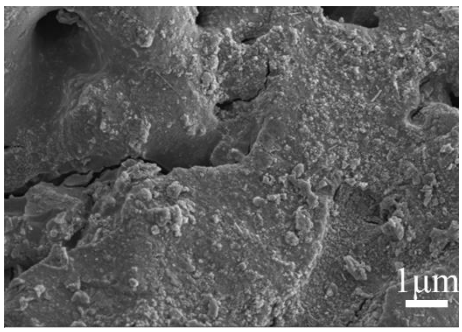

Fig. 20. SEM images of Fe_2O_3/geopolymer porous ceramic samples after adsorption of Pb(II)

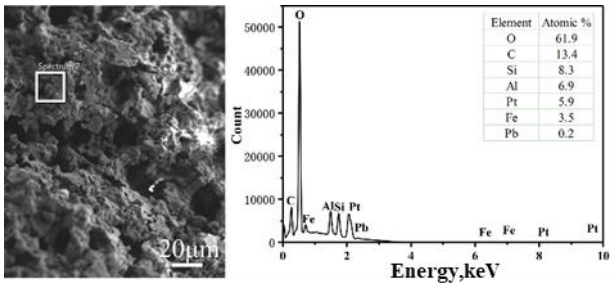

Fig. 21. SEM- EDS images of Fe_2O_3/geopolymer porous ceramic samples after adsorption of Pb(II)

After adsorption of Pb(II), some small tablet-like particles appeared on the surface of the sample, which may be adsorbed lead compounds. Meanwhile, the elemental peaks of Pb appeared in the EDS patterns, indicating that Pb(II) was successfully adsorbed on the surface of the samples.

3.4. Investigation of the mechanism of Pb(II) adsorption of Fe_2O_3/geopolymer porous ceramic samples

3.4.1. FTIR analysis

FTIR patterns of geopolymer porous ceramic samples before and after loading with Fe_2O_3, as well as the FTIR pattern of Fe_2O_3/geopolymer porous ceramic samples after adsorption of Pb(II) are shown in Fig. 22.

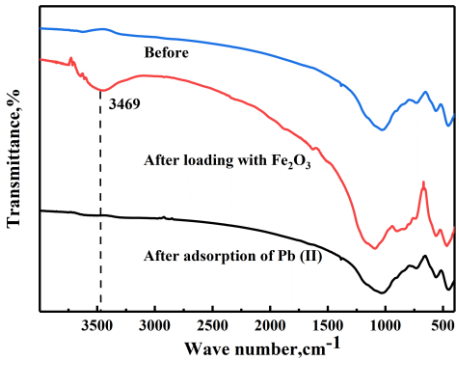

Fig. 22. FTIR patterns of geopolymer porous ceramic samples before and after loading with Fe_2O_3 and Fe_2O_3/geopolymer porous ceramic samples after adsorption of Pb(II)

There were a large number of hydroxyl (-OH) groups in the region of 3469 cm^{-1} after loading with Fe_2O_3, which relate to the large number of -OH groups distributed on the surface of Fe_2O_3 [21]. These -OH groups can improve the hydrophilicity of the surface of samples and achieve better Pb(II) adsorption performance of the samples. After adsorption of Pb(II), the peak of the -OH group disappeared, indicating that the -OH groups on the surface of samples underwent a complexation reaction with Pb(II). The -OH groups were consumed during the adsorption process. This is consistent with the results observed by Wang [22] et al.

3.4.2. XPS analysis

The survey XPS pattern of the samples before and after loading with Fe_2O_3 and the Fe_2O_3/ geopolymer porous ceramic samples after adsorption of Pb(II) are shown in Fig. 23. A peak of Fe emerged after loading with Fe_2O_3, indicating that Fe element was present on the surface of samples. The peak of Pb emerged in the patterns after adsorption of Pb(II), indicating that Pb(II) was successfully adsorbed on the surface of the samples.

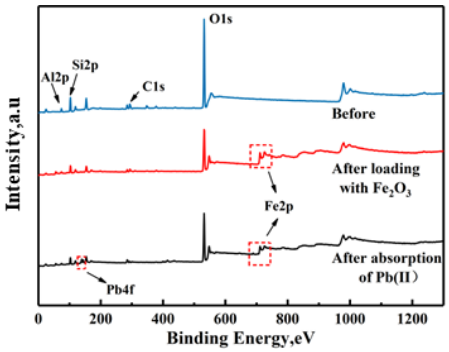

Fig. 23. Survey XPS pattern of geopolymer porous ceramic samples before and after loading with Fe_2O_3 and Fe_2O_3/geopolymer porous ceramic samples after adsorption of Pb(II)

The high-resolution XPS pattern of Fe2p before and after adsorption is shown in Fig. 24 a. Fe2p exhibits two peaks assigned to $Fe2p_{3/2}$ and $Fe2p_{1/2}$ with the binding energies of 711.15 eV and 724.35 eV before adsorption. The spin orbit splitting energy difference of these two peaks is about 13.2 eV, and two satellite peak locates at 719.9 eV and 733.01 eV, indicating that the iron oxide loaded on the surface of samples is mainly Fe_2O_3 [22, 23]. And the peaks with binding energies of 716.35 eV belong to Fe (III) [24].The position of the $Fe2p_{3/2}$ peak did not change while the $Fe2p_{1/2}$ peak shifted towards a higher binding energy after the adsorption of Pb(II), indicating that the occurrence of charge transfer from Fe during the adsorption process.

The high-resolution XPS pattern of Pb4f is shown in Fig. 24 b. Pb4f exhibits two peaks assigned to $Pb4f_{7/2}$ and $Pb4f_{5/2}$ with binding energies of 138.5 eV and 143.45 eV. The binding energy of $Pb4f_{7/2}$ is lower than $Pb(NO_3)_2$ (139.7 eV), indicating that Pb(II) tended to acquire or share electrons during the adsorption process, which may be relate to the complexation reaction between Pb(II) and the surface functional groups of Fe_2O_3.

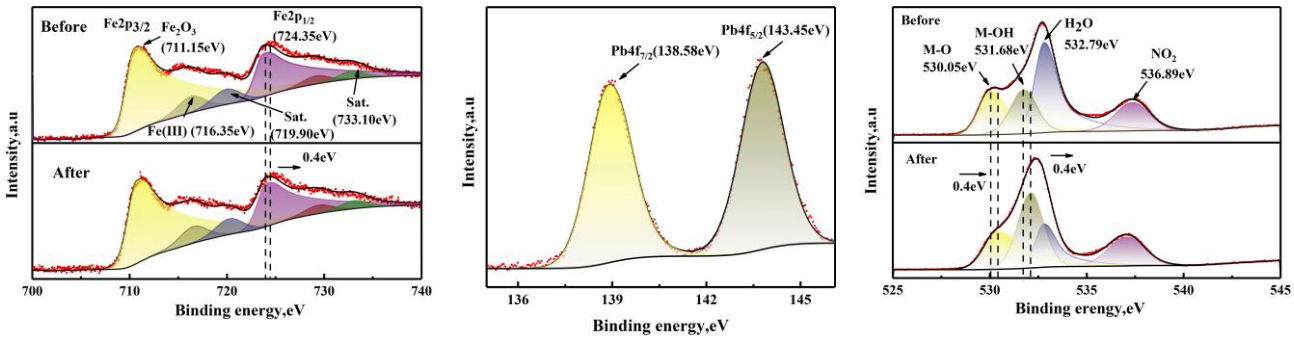

a b c

Fig. 24. High-resolution XPS patterns: a – Fe2p before and after adsorption of Pb(II); b – Pb4f after adsorption of Pb(II); c – O1s before and after adsorption of Pb(II)

The high-resolution XPS patterns of O1s before and after adsorption of Pb(II) are shown in Fig. 24 c, three peaks with binding energies of 530.05 eV, 531.68 eV, and 532.79 eV belong to M-O (M refer metallic element), M-OH and H_2O [**Error! Reference source not found.**]. The p eak with a binding energy of 536.89 eV belongs to the NO_2 [26] remaining on the surface of the sample after the decomposition of $Fe(NO_3)_3$. As shown in Fig. 24 c, it can be observed that the peak of M-O shifted towards the high binding energy. The peak area of M-O decreased after adsorption, indicating that a reaction occurred between Fe-O and Pb(II) during the adsorption process, and the Fe-O was consumed. The peak area of M-OH after adsorption increased compared to before, and the peak of M-OH also shifted towards high binding energy. The M-OH tended to lose electrons, indicating that Pb(II) coordinated with the M-OH on the surface of samples and generated $Pb(OH)_2$. Thus, the peak area of M-OH increased.

4. CONCLUSIONS

The following conclusions are drawn:

1. With the increase of sintering temperature, the amorphous geopolymer gradually transformed into geopolymer ceramics mainly composed of leucite and anorthite phases. Meanwhile, the porosity of geopolymer porous ceramic samples and the pore size of internal pores gradually decreased, and the compressive strength gradually increased.
2. The Fe_2O_3/geopolymer porous ceramic samples prepared by impregnating with 0.2M $Fe(NO_3)_3$ solution and drying, final calcining at 450 ℃ for 2 hours had the best adsorption performance with an adsorption capacity of 1.94 mg/g. The Fe_2O_3 particles on the surface of samples had a moderate particle size, and it distributed uniformly on the surface of samples. The adsorption capacity increased with the increasing solution pH value, from 0.16 mg/L at solution pH = 1.47 to 1.99 mg/L at pH = 6.5. The adsorption capacity increased with the increasing initial concentration of Pb(II), from 0.90 mg/g when the initial concentration of Pb(II) was 20 mg/L to 2.79 mg/g when the initial concentration of Pb (II) was 100 mg/L.
3. Pb(II) adsorption mechanism of Fe_2O_3/geopolymer porous ceramic samples was electrostatic adsorption and complexation reaction between the surface functional groups of samples and Pb(II).

Acknowledgments

This research was supported by the development and application of hygroscopic materials suitable for hot summer and cold winter areas grant funded by Anhui Jianzhu University (No. JY2021-C-125).

REFERENCES

1. **Bushra, K., Abdul, R.** A Mini Review of Treatment Methods for Lead Removal from Wastewater *International Journal of Environmental Analytical Chemistry* 103 (17) 2023: pp. 5126 – 5141. https://doi.org/10.1080/03067319.2021.1934833
2. **Kaviyarasi, R., Rituraj, C., Haritha, M., Rajeshwari, K., Ademola, C.F., Harishkumar, H., Vellingiri, B., George, Alex., Gopalakrishnan, A.V.** Molecular Mechanism of Heavy Metals (Lead, Chromium, Arsenic, Mercury, Nickel and Cadmium)-Induced Hepatotoxicity-A-Review *Chemosphere* 271 2021: pp. 129735. https://doi.org/10.1016/j.chemosphere.2021.129735
3. **Chen, Q.Y., Yao, Y., Li, X.Y, Zhou, J., Huang, Z.L.** Comparison of Heavy Metal Removals from Aqueous Solutions by Chemical Precipitation and Characteristics of Precipitates *Journal of Water Process Engineering* 26 2018: pp. 289 – 300. https://doi.org/10.1016/j.jwpe.2018.11.003
4. **Pan, S.Y., Shen, Z.D., Zhang, X.L., Pang, B.C.** Metastable Nano-Zirconium Phosphate Inside Gel-Type Ion Exchanger for Enhanced Removal of Heavy Metals *Journal of Hazardous Materials* 423 (b) 2022: pp. 127158. https://doi.org/10.1016/j.jhazmat.2021.127158
5. **Zheng, B., Chu, X.X., Peng, Z., Tian, Y.M.** Improving the Separation Performance for Heavy Metals by Optimizing the Structure of Multilayered GO Membrane *Journal of Molecular Liquids* 370 2023: pp. 121071. https://doi.org/10.1016/j.molliq.2022.121071
6. **Malik, L.A., Bashir, A., Qureashi, A.** Detection and Removal of Heavy Metal Ions: A Review *Environmental Chemistry Letters* 17 2019: pp. 1495 – 1521. https://doi.org/10.1007/s10311-019-00891-z
7. **Wang, Z., Luo, P.P., Xu, C.Y., Kang, S.X., Zhou, M.M.,** Overview Assessment of Risk Evaluation and Treatment Technologies for Heavy Metal Pollution of Water and Soil *Journal of Cleaner Production* 379 (2) 2022: pp. 34043. https://doi.org/10.1016/j.jclepro.2022.134043
8. **Jeirani, Z., Niu, C.H., Soltan, J.** Adsorption of Emerging Pollutants on Activated Carbon *Reviews in Chemical*

Engineering 33 (5) 2017: pp. 491 – 522.
https://doi.org/10.1515/revce-2016-0027

9. **Seef, S.F., Mohammed, A.A., Wan, Z.J.** Review on Heavy Metal Adsorption Processes Carbon Nanotubes *Journal of Cleaner Production* 230 2019: pp. 783 – 793.
https://doi.org/10.1016/j.jclepro.2019.05.154
10. **Martín, E.G., César, M.L., Aida, A.P., Jorge, R.R.** Calculating Adsorption Efficiencies and Reusability Cycles by Retrieving the Concept of Operating Lines *Separation Science and Technology* 57 (17) 2022: pp. 2708 – 2717.
https://doi.org/10.1080/01496395.2022.2042020
11. **Dina, E., Muneer, M.B., Abdelbaki, B., Muftah, H.E.** Adsorption of Organic Water Pollutants by Clays and Clay Minerals Composites: A Comprehensive Review *Applied Clay Science* 229 2022: pp. 106686.
https://doi.org/10.1016/j.clay.2022.106686
12. **Sonia, R., Ana, G., Edgar, G., Eudald, C., Victor, P.** Use of CeO_2, TiO_2 and Fe_3O_4 Nanoparticles for The Removal of Lead from Water: Toxicity of Nanoparticles and Derived Compound *Desalination* 277 (1 – 3) 2011: pp. 213 – 220.
https://doi.org/10.1016/j.desal.2011.04.036
13. **Zhang, T.Y., Liu, J.D., Zhou, F., Zhou, S.Y., Wu, J.C.** Polymer-Coated Fe_2O_3 Nanoparticles for Photocatalytic Degradation of Organic Materials and Antibiotics in Water *ACS Applied Nano Materials* 3 (9) 2020: pp. 9200 – 9208.
https://doi.org/10.1021/acsanm.0c01829
14. **Liu, X.Q., Zhao, X.X., Liu, Y.** Review on Preparation and Adsorption Properties of Chitosan and Chitosan Composites *Polymer Bulletin* 79 2022: pp. 2633 – 2665.
https://doi.org/10.1007/s00289-021-03626-9
15. **Yan, S., Zhang, F.Y., Wang, S., He, P.G., Jia, D.C.** Crystallization Behavior and Mechanical Properties of High Open Porosity Dolomite Hollow Microspheres Filled Hybrid Geopolymer Foams *Cement and Concrete Composites* 104 2019: pp. 103376.
https://doi.org/10.1016/j.cemconcomp.2019.103376
16. **Bell, J.L., Driemeyer, P.E., Kriven, W.M.** Formation of Ceramics from Metakaolin-Based Geopolymers. Part II: K-Based Geopolymer *Journal of the American Ceramic Society* 92 2009: pp. 607 – 615.
https://doi.org/10.1111/j.1551-2916.2008.02922.x
17. **Peter, D., Grant, C.L., Jannie, S.J.** Thermal Evolution of Metakaolin Geopolymers: Part 1-Physical Evolution *Journal of Non-Crystalline Solids* 352 (52 – 54) 2006: pp. 5541 – 5555.
https://doi.org/10.1016/j.jnoncrysol.2006.09.019
18. **Kobayashi, Y., Kato, E.** Low-Temperature Fabrication of Anorthite Ceramics *Journal of the American Ceramic Society* 77 (3) 1994: pp. 833 – 834.
https://doi.org/10.1111/j.11512916.1994.tb05373.x
19. **He, P.G., Jia, D.C., Wang, S.** Microstructure and Integrity of Leucite Ceramic Derived from Potassium-Based Geopolymer Precursor *Journal of the European Ceramic Society* 33 2013: pp. 689 – 698.
https://doi.org/10.1016/j.jeurceramsoc.2012.10.019
20. **Da Silva, C.P., dos Santos, A.V., Oliveira, A.S.** Synthesis of Composites and Study of The Thermal Behavior of Sugarcane Bagasse/Iron Nitrate Mixtures in Different Proportions *Journal of Thermal Analysis and Calorimetry* 131 2018: pp. 611 – 620.
https://doi.org/10.1007/s10973-017-6260-1
21. **Hiroki, T., Kenya, M., Akio, T., Makoto, I.** Mechanism of Hydroxylation of Metal Oxide Surfaces *Journal of Colloid and Interface Science* 243 (1) 2001: pp. 202 – 207.
https://doi.org/10.1006/jcis.2001.7864
22. **Wang, H.T., Sun, W.S., Liang, X., Zou, H.Y., Jiao, Y.** Two-Dimensional Fe_2O_3 Nanosheets as Adsorbent for The Removal of Pb(II) from Aqueous Solution *Journal of Molecular Liquids* 335 2021: pp. 116197.
https://doi.org/10.1016/j.apsusc.2007.09.063
23. **Yamashita, T., Peter, H.** Analysis of XPS Spectra of Fe^{2+} and Fe^{3+} Ions in Oxide Materials *Applied Surface Science* 254 (8) 2008: pp. 2441 – 2449.
https://doi.org/10.1016/j.apsusc.2007.09.063
24. **Tang, S.F., Zhou, H., Tan, W.T., Huang, G.J., Zeng, P., Gu, J.F., Liao, B.H.** Adsorption Characteristics and Mechanisms of Fe-Mn Oxide Modified Biochar for Pb(II) in Wastewater *International Journal of Environmental Research and Public Health* 19 2022: pp. 8420.
https://doi.org/10.3390/ijerph19148420
25. **Yin, G.C., Song, X.Y., Tao, L. Sarkar, B., Sarmah, A.K.** Novel Fe-Mn Binary Oxide-Biochar as An Adsorbent for Removing Cd(II) from Aqueous Solutions *Chemical Engineering Journal* 389 2020: pp. 124465.
https://doi.org/10.1016/j.cej.2020.124465
26. **Sharma, L., Matsuoka, T., Kimura, T., Matsuda, H.** Investigation into The Surface Relief Grating Mechanism via XPS in New Azobenzene Based Optical Material *Polymers for Advanced Technologies* 13 (6) 2002: pp. 481 – 486.
https://doi.org/10.1002/pat.214